Physics and Chemistry of Minerals (2020) 47:9
https://doi.org/10.1007/s00269-019-01078-2

ORIGINAL PAPER

Crystal structure of impurity-free rhodochrosite ($MnCO_3$) and thermal expansion properties

Wen Liang[1] · Lin Li[2,6] · Rui Li[1,3] · Yuan Yin[1,3] · Zeming Li[1,3] · Xiqiang Liu[1,3] · Shuangmin Shan[1] · Yu He[1] · Yong Meng[4] · Zengsheng Li[5] · Heping Li[1]

Received: 22 July 2019 / Accepted: 30 November 2019 / Published online: 13 January 2020

Abstract

To explain the anomalous anisotropy in thermal expansion properties reported in rhodochrosite ($MnCO_3$) previously Rao and Murthy (J Mater Sci 5: 82, 1970), Li et al. (High Temp High Press, 2019), the evaluation of crystal structure is thought to be indispensable as an important aspect in mineralogy. In this spirit, single crystals of impurity-free rhodochrosite, up to 100 µm in size, were synthesized under high-pressure–temperature (*P*–*T*) conditions. The standard crystal structure, without the impurities common to natural samples, was investigated by means of single-crystal X-ray diffraction (XRD). The unit cell parameters obtained for the $R\bar{3}c$ symmetry were $a = 4.7754(5)$ Å and $c = 15.6484(18)$ Å, with a final *R* value of 0.0162. The (MnO_6) octahedron exhibits an anomalous bond angle that tends more toward 90° of a regular octahedron, which is totally different from those of $MgCO_3$, $FeCO_3$, and $CaCO_3$. Using the single-crystal XRD from 100 to 370 K, the thermal expansion coefficients were quantified as $\alpha_a = 5.08 \times 10^{-6}$ K^{-1} and $\alpha_c = 18.06 \times 10^{-6}$ K^{-1}, as well as $\alpha_{V\text{unit cell}} = 28.49 \times 10^{-6}$ K^{-1}. The geometry of (MnO_6) octahedron as function of temperature was also determined as $\alpha_{\text{Mn–O}} = 12.14 \times 10^{-6}$ K^{-1} and $\alpha_{\text{O–Mn–O}} \approx 0.05°$/100 K. The anisotropy of $MnCO_3$ ($\alpha_a/\alpha_c = 3.55$), similar to that of $MgCO_3$ (~3.0, Markgraf and Reeder, Am Mineral, 70: 590–600, 1985), indicates that the difference in bond angle has no significant effect on the thermal expansion properties. According to the standard crystal structures of end members ($MgCO_3$, $FeCO_3$, $MnCO_3$, and $CaCO_3$), the cation substitution in calcite-type structures is proven to agree with the rigid body model and the linear solid solution relationship is highly consistent with those of natural carbonates.

Keywords Impurity-free rhodochrosite single crystal · Crystal structure · Single-crystal XRD · Thermal expansion

Introduction

An essential goal of geoscience is to establish exact mineralogical models for enhancing our current understanding of the physical and chemical interactions that occur between Earth's most abundant minerals. Carbonates with various compositions are attractive in this regard because

Wen Liang and Lin Li contributed equally to this work.

Electronic supplementary material The online version of this article (https://doi.org/10.1007/s00269-019-01078-2) contains supplementary material, which is available to authorized users.

✉ Wen Liang
liangwen@mail.gyig.ac.cn

✉ Heping Li
liheping@vip.gyig.ac.cn

[1] Key Laboratory of High Temperature and High Pressure Study of the Earth's Interior, Institute of Geochemistry, Chinese Academy of Sciences, Guiyang 550081, China

[2] State Key Laboratory of Geological Processes and Mineral Resources, China University of Geosciences, 29 Xueyuan Road, Beijing 100083, China

[3] University of Chinese Academy of Sciences, Beijing 100049, China

[4] State Key Laboratory of Ore Deposit Geochemistry, Institute of Geochemistry, Chinese Academy of Sciences, Guiyang 550081, China

[5] Shandong Geological Sciences Institute, Jinan 250013, China

[6] Institute of Science Research, China University of Geosciences, Beijing 100083, China

they are widely distributed and participate in many geological processes (Javoy 1997; Seto et al. 2008; Oelkers and Cole 2008; Litasov and Ohtani 2009; Ma et al. 2018; Duan et al. 2019). In particular, interest in carbonates has grown significantly in regard to their involvement in the global carbon cycle, which is the subject of ongoing debate (Dasgupta and Hirschmann 2010; Hazen et al. 2012). Till now, extensive research on calcite–dolomite–magnesite systems ($(Ca,Mg)CO_3$) has been conducted because they are likely to be the dominant carbonates in the Earth's crust (Markgraf and Reeder 1985; Reeder and Dollase 1989; Williams et al. 1992; Biellmann et al. 1993; Gillet et al. 1993; Fiquet et al. 1994; Suito et al. 2001; Ono et al. 2007; Ishizawa et al. 2013). Comprehensive investigation of the high *P*–*T* properties of ferromagnesite systems ($(Mg,Fe)CO_3$) is of great importance in understanding the deep-carbon storage characteristics of the Earth's interior (Isshiki et al. 2004; Lavina et al. 2009; Lin et al. 2012; Liu et al. 2014; Spivak et al. 2014; Cerantola et al. 2015, 2017; Merlini et al. 2016; Liang et al. 2018a, b). On the opposite, the phase behavior and properties of rhodochrosite ($MnCO_3$) have attracted much less attention than those of calcite, magnesite, and siderite, because of the relatively low abundance on Earth (Liu et al. 2001; Santillan and Williams 2004; Ono 2007; Farfan et al. 2013; Merlini et al. 2015; Liu et al. 2016).

However, some anomalous features in the physical properties of rhodochrosite are noteworthy from previous studies. Typically, rhodochrosite has a bulk modulus ($K_0 = 106.9$ GPa for $K' = 4$, Merlini et al. 2015; $K_0 = 113$ GPa for $K' = 4$, Liu et al. 2016) nearly equal to that of magnesite ($K_0 = 103$ GPa for $K' = 4$, Zhang et al. 1997; $K_0 = 111$ GPa for $K' = 4$, Ross 1997) but is much larger than that of siderite ($K_0 = 97.5$ GPa for $K' = 4$, Liang et al. 2018b). These results cannot be explained in terms of general compression mechanisms because rhodochrosite has the longest Mn–O bond length (Hazen and Finger 1982). Likewise, rhodochrosite has highly anisotropic thermal expansion [$\alpha_c/\alpha_a = \sim 6.0$, Li et al. 2019 (in press)], while it is ~ 2.5 for siderite (Liang et al. 2018c) and ~ 3.0 for magnesite (Markgraf and Reeder 1985). According to the existing literature (Megaw 1971; Ross 1997), the (AO_6) octahedron geometry in calcite-type structures has possible consequences on elasticity and thermal expansion. It is thus conceivable that the thermal expansion properties of (MnO_6) octahedron could be quite different from those of magnesite and siderite, thereby causing the anomalous anisotropy; however, this remains largely unclear from the previous powder XRD results. Previous reports have focused on natural rhodochrosite with low purity (~ 95%) such that the geometry of (MnO_6) octahedron is impossible to quantify because of the interference of Ca^{2+}, Mg^{2+}, and Fe^{2+} impurities (Effenberger et al. 1981; Maslen et al. 1995). Exactly, the geometry of standard (MnO_6) octahedron from impurity-free rhodochrosite becomes an important criterion of evaluating the distortion of (MnO_6) octahedron in Mn-bearing carbonates [e.g., kutnohorite $CaMn(CO_3)_2$, norsethite-type $BaMn(CO_3)_2$, etc.]. For this reason, synthetic sample is necessary; nevertheless, single crystal growth of impurity-free rhodochrosite has not been reported yet. In addition, natural calcite-type carbonates are generally identified as complex solid solutions composed of four major end members: $CaCO_3$, $MgCO_3$, $FeCO_3$, and $MnCO_3$. Owing to proper differences in ionic radii (Reeder et al. 1983), $MgCO_3$, $FeCO_3$, and $MnCO_3$ can form complete solid solutions (Rosenberg 1963), which also applies to the case for small amounts of Ca^{2+}. According to the Vegard's law, correspondence between lattice parameters and the composition of calcite-type carbonates, such as binary, ternary, and quaternary, can be quantified by the weighted sum of each end member. Accordingly, knowledge of the standard crystal structure of rhodochrosite is indispensable, as it has the same research value as other end members in defining a quantitative carbonate model.

To clarify these issues, single crystals of impurity-free rhodochrosite were synthesized under high-*P*–*T* conditions and its crystal structure was determined by single-crystal XRD. Using each end member as a node, a linear solid solution model was established for carbonates to quantify the relationship between the structure and composition. Using the single-crystal XRD at different temperatures, the accurate thermal expansion coefficient of lattice parameters, bond length, and bond angle were quantified.

Experimental method

Single crystals of rhodochrosite were grown by high-*P*–*T* annealing in a sealed cavity, as reported by Liang et al. (2018b). The high-*P*–*T* experiments were performed on a DS 6 × 600t cubic-anvil-type apparatus using graphite heater and h-BN as pressure medium. The first step is for crystal nucleation: $MnCO_3$ powder (analytical reagent 99.99%, Alfa Aesar) and anhydrous $H_2C_2O_4$ (98%, Alfa Aesar) were mixed at molar ratio 1:1. A sample pellet of 6 mm diameter and 3 mm length was prepared and sealed in a platinum tube (0.1 mm thickness) with 30 μL deionized water. The high *P*–*T* annealing was performed at 3 GPa and 700 °C for 6 h, and then it was quenched to room temperature and the pressure released. The platinum capsule was cut open and the small crystals of 10–20 μm in sizes were obtained. The second step for crystal growth: $MnCO_3$ powder and anhydrous $H_2C_2O_4$ were mixed as 1:0.1 molar ratio, and then mixed with the small crystals (1:3 molar ratio of $MnCO_3$ small crystals: $MnCO_3$ powder) and sealed in a platinum capsule with 30 μL deionized water. The sample was retreated under 3 GPa and 700 °C for 24 h, and then quenched to ambient conditions. The platinum capsule was opened and

the sample was removed, cleaned with alcohol by ultrasonication and air-dried. The single crystals were observed under a plane-polarized microscope and the micro-composition was quantified by electron probe analysis.

Single-crystal XRD measurements were obtained at ambient conditions with a Rigaku Xtalab PRO diffractometer system and HyPix-6000HE detector. The intensity data were collected using a 1.2 kW water-cooled microfocus source with a Mo rotor target and multilayer mirrors. Data processing was performed with the CrysAlisPro processing program. The structures were determined using direct methods with the SHELXS package and refined in the anisotropic approach for non-hydrogen atoms using the SHELXL program (Sheldrick 2008). For various temperatures, the selected perfect single crystal has been mounted on a glass fiber. The temperature was controlled and measured by a set of Oxford Cryosystems; by blowing cooled and heated N_2 gas onto the sample, the sample's temperature can be fixed at the given temperatures. The single-crystal data were obtained from cooled or heated sample after 30 min stabilization, to maintain a thermal equilibrium state of the sample. Measurements for all the variation temperature experiments were conducted from 100 to 370 K.

Results and discussion

Single-crystal growth and characterization of impurity-free rhodochrosite

$MnCO_3$ analytical reagent is ready-made for experimental research but single crystals of impurity-free rhodochrosite are currently unavailable. Rhodochrosite crystals were cultivated in CO_2 acidic aqueous solutions under high *P–T* via crystal nucleation and crystal growth. $MnCO_3$ could grow rapidly into crystal nuclei (10–20 μm) in a $CO_2 + H_2O$ acid medium within 6 h; in comparison, $FeCO_3$ requires 12 h under the same conditions (Liang et al. 2018b), revealing that $MnCO_3$ has much faster growth rates than $FeCO_3$. Subsequently, the crystal nuclei were used as seeds for crystal growth. The key to this process is to drastically reduce the nominal concentration of CO_2 in the closed cavity. The purpose is to inhibit the continuous development of tiny crystal nuclei while helping the added seeds grow into large crystals. Otherwise, if crystal nucleation and crystal growth occur simultaneously, some inclusions of tiny crystals appear in the large crystals, thereby lowering the quality of the single crystals. To illustrate the oxygen fugacity condition, a trial decomposition reaction of $MnCO_3$ in the same assembly was carried out at 0.2 GPa and 700 °C for 1 h. The product was identified as a mixture of $MnCO_3$ and MnO by powder XRD, as seen in Supplementary Fig. 1. The presence of MnO, and not Mn_3O_4, provides direct evidence that oxygen fugacity ensures the stability of Mn^{2+} in $MnCO_3$.

From optical microscope observations, the single crystals of rhodochrosite up to 100 μm in sizes exhibited a rhombohedral habit with perfect (101) cleavage, as seen in Fig. 1. Several inclusions of tiny crystals were observed; nevertheless, the single crystals were large enough and could be cut into several pieces. A piece of ~ 50-μm crystal without any inclusions was selected for single-crystal XRD measurement. A thin section was prepared from the rhodochrosite crystals and used for electron probe analysis. A backscattering electronic image of the thin section with the detection position and the results of Mn content analysis are given in Fig. 2 and Table 1. The grayscale of backscattered electron image had no distinction, therefore, indicating that the chemical composition was homogeneous. A total of 15 points in five different areas were selected for electron probe analysis and the average MnO wt% was 61.70 ± 0.05%. Thus, the composition of the crystals was calculated to be $Mn_{1.0002\pm0.0010}CO_3$, in good agreement with ideal chemical formula.

Rhodochrosite, also known as Inca Rose, is an important kind of carbonate gemstone with a typically rose-red color. Based on our experiment, rhodochrosite crystals were proven to grow easily from $MnCO_3$ powder in $CO_2 + H_2O$ environment under high *P–T*. On this basis, 100-μm crystals we obtained could be used as seeds to cultivate much larger sized crystals in an autoclave using relatively low *P–T* and a long growth time. It could provide a reference for the artificial growth of Inca Rose gemstones.

The crystal structure of impurity-free rhodochrosite

The crystal structure of rhodochrosite was determined by single-crystal XRD. The crystal data and structural refinement, including the lattice parameters, positional and thermal properties, and bond length and angle, are summarized in Table 2, together with magnesite, siderite, and calcite for comparison (Markgraf and Reeder 1985; Liang et al 2018a, b), as well as the natural carbonates reported by Effenberger et al. (1981). Differences in lattice parameters between synthetic samples and natural samples are caused by the influence of impurities. The result was formatted into a CIF file that is attached as supplementary material. As shown in Fig. 3a, calcite-type carbonates (ACO_3) have a common $R\bar{3}c$ rhombohedral structure (Graf 1961). The carbonate ions (CO_3^{2-}) are characterized by strong internal C–O bonds, interlinked with the cations A by weaker A–O bonds. The central ion A is six-coordinated in a slightly tilting (AO_6) octahedron with six equal A–O bond lengths. A variable O–A–O angle corresponding to the deviation from the regular octahedron (O–A–O = 90°) results from hybridization between the A and O valence electronic orbitals.

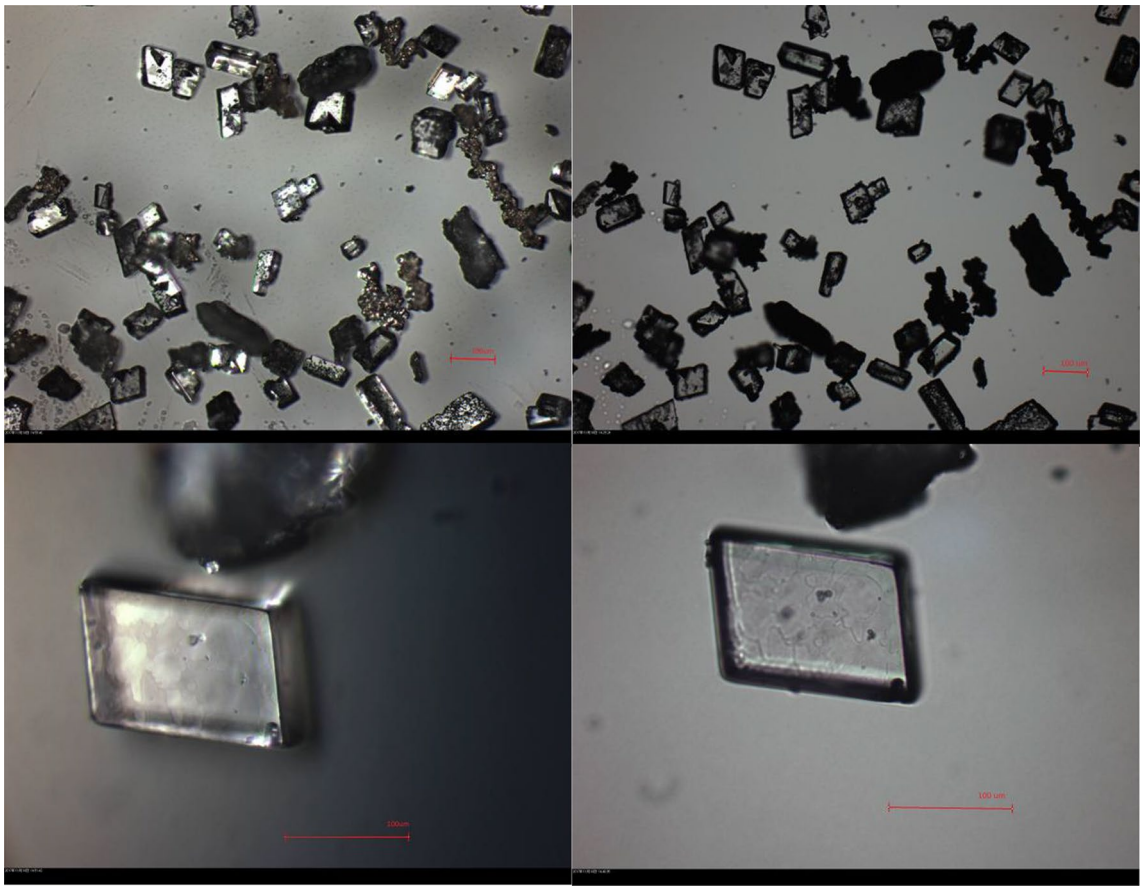

Fig. 1 The micrographs of $MnCO_3$ single crystals under plane-polarized microscope with reflected light and transmitted light

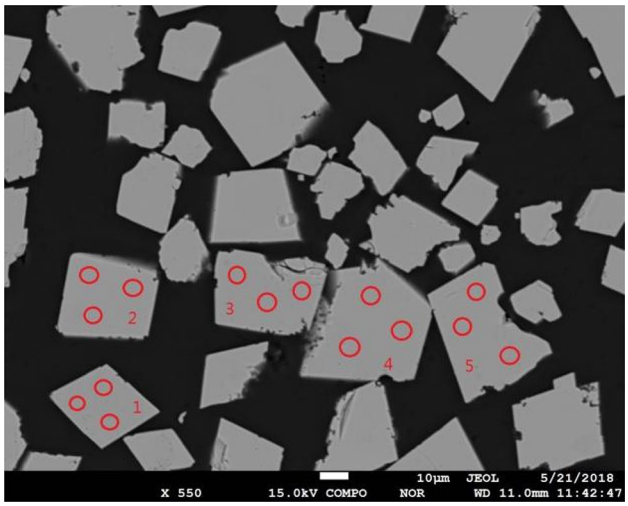

Fig. 2 Backscattered electrons image of $MnCO_3$ single crystals, in which the red circles are the positions where analyses were performed

Effenberger et al. (1981) modeled calcite-type structures and obtained important results for the field of crystal chemistry, subsequently providing a basic reference for the carbonates research. However, limited by the conditions at that time, natural samples with trace impurities had to be used for research. Till now, the standard crystal structures of magnesite, siderite, and rhodochrosite have been achieved from the impurity-free crystals (Liang et al. 2018a, b). In this case, the calcite-type model can be further optimized in aspects of avoiding the impurities influence completely. We used the Shannon effective ionic radius as a physical quantity to objectively describe the cation substitution in the calcite-type lattice (Shannon and Prewitt 1969). Figure 3b gives the variation in unit cell volume with increasing ionic radii, in which the behavior of four end members obeys a linear relationship (with a correlation of $R^2 = 0.9998$):

$$V_{\text{unit cell}} = 44.394 + 323.192 \times r.$$

The large slope of this relationship (323.192) reveals that the cation substitution is of decisive significance to the calcite-type lattice.

This near-perfect linear relationship provides strong evidence that the rigid body model is valid for simulating the substitution of various cations in the calcite-type lattice. According to Vegard's law, the unit cell parameters

Table 1 Composition of the rhodochrosite crystals used in our study

MnO wt%	Position 1	Position 2	Position 3	Average	Standard deviation
Region 1	61.63	61.58	61.74	61.65	0.08
Region 2	61.81	61.75	61.63	61.73	0.09
Region 3	61.74	61.69	61.82	61.75	0.07
Region 4	61.79	61.66	61.73	61.73	0.07
Region 5	61.72	61.68	61.59	61.66	0.07
Composition	–	–	–	61.70 ± 0.05	$Mn_{1.0002\pm0.0010}CO_3$

Table 2 Single-crystal structural parameters of rhodochrosite and other calcite-type carbonates

	References	*a*	*c*	*α*	*β*	*γ*	*V*	A–O	C–O	O–A–O
Space group $R\bar{3}c$										
Lattice parameters										
Rhodochrosite	Synthetic sample This study	4.7754 (5)	15.6484 (18)	90	90	120	309.04 (8)	2.1945 (9)	1.2855(17)	88.30 (2)
	Natural sample $Mn_{0.929}Fe_{0.065}Mg_{0.004}Ca_{0.002}CO_3$ Effenberger et al. (1981)	4.7682 (2)	15.6354 (8)	90	90	120	307.86 (4)	2.1900 (5)	1.2867 (5)	–
Magnesite	Synthetic sample Liang et al. (2018a)	4.6255 (3)	14.987 (2)	90	90	120	277.69 (4)	2.0976 (4)	1.2846 (7)	88.179 (11)
	Natural sample $Mg_{0.986}Fe_{0.010}Ca_{0.002}Mn_{0.002}CO_3$ Effenberger et al. (1981)	4.6328 (2)	15.0129 (5)	90	90	120	279.05 (3)	2.1018 (4)	1.2852 (4)	–
Siderite	Synthetic sample Liang et al. (2018b)	4.6861 (3)	15.362 (2)	90	90	120	292.15 (5)	2.141 (2)	1.287 (4)	87.92 (5)
	Natural sample $Fe_{0.948}Mn_{0.047}Mg_{0.004}Ca_{0.002}CO_3$ Effenberger et al. (1981)	4.6916 (4)	15.3796 (16)	90	90	120	293.17 (8)	2.1445 (5)	1.2869 (5)	–
Calcite	Natural sample $Ca_{0.998}Mg_{0.002}CO_3$ Markgraf and Reeder (1985)	4.988 (1)	17.061 (1)	90	90	120	376.60 (8)	2.3595 (4)	1.2804 (7)	87.444 (5)
	Natural sample $Ca_{0.994}Mg_{0.004}Fe_{0.002}CO_3$ Effenberger et al. (1981)	4.9896 (2)	17.0610 (11)	90	90	120	367.85 (5)	2.3598 (6)	1.2815 (6)	–

Parameters	Mn		C		O	
Positional and thermal parameters of rhodochrosite						
x	0		0		0.2692 (3)	0.26986 (9)[a]
y	0		0		0	
z	0		0.25		0.25	
U_{11}	0.0073 (4)	0.00662 (8)[a]	0.0091 (12)	0.00632 (22)[a]	0.0074 (6)	0.00634 (12)[a]
U_{22}	0.0073 (4)	0.00662 (8)[a]	0.0091 (12)	0.00632 (22)[a]	0.0106 (8)	
U_{33}	0.0091 (4)	0.00624 (9)[a]	0.0057 (16)	0.00572 (35)[a]	0.0130 (9)	0.01024 (16)[a]
U_{23}	0.0000		0.0000		− 0.0030 (6)	
U_{13}	0.0000		0.0000		− 0.0015 (3)	− 0.00108 (6)[a]
U_{12}	0.00367 (18)		0.0045(6)		0.0053 (4)	0.00485 (8)[a]

[a]Parameters of natural rhodochrosite given by Effenberger et al. (1981)

vary linearly with composition. Using each impurity-free end member as a node, a linear solid solution model can be established to calculate the theoretical relationship between lattice parameters and composition. That is, the unit cell volume of the solid solution is approximately equal to the weighted sum of the end members, described as

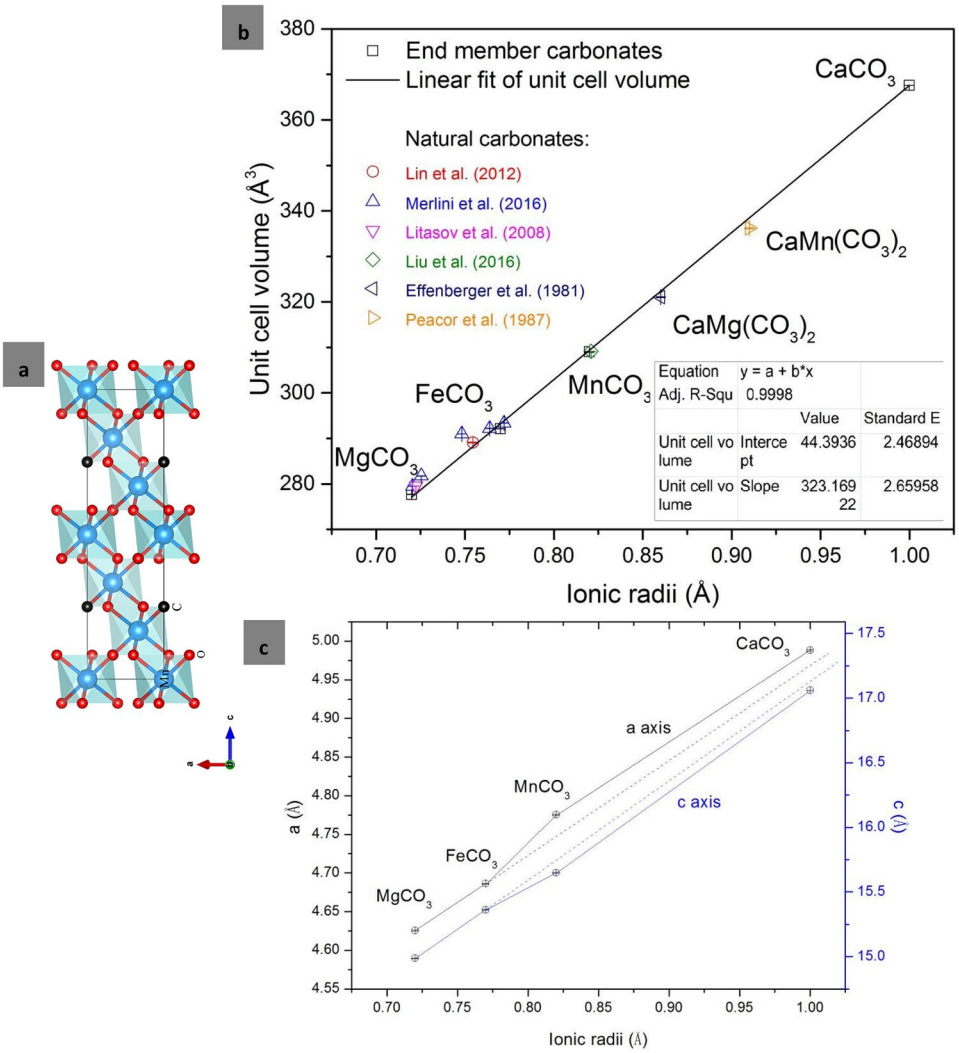

Fig. 3 **a** Crystal structure of $MnCO_3$ (space group $R\bar{3}c$) representative of the structure of all the calcite-type carbonates. **b** The variation of unit cell volume with ionic radii, in which the data of end member carbonates come from $MgCO_3$ (Liang et al. 2018a), $FeCO_3$ (Liang et al. 2018b), $MnCO_3$ (this work), and $CaCO_3$ (Markgraf and Reeder 1985), respectively. **c** The nonlinear relationship of lattice parameters *a* and *c* as the function of ionic radii

$$\mathrm{Mg}_{X_1}\mathrm{Fe}_{X_2}\mathrm{Mn}_{X_3}\mathrm{Ca}_{X_4}\mathrm{CO}_3,$$

$$X_1 + X_2 + X_3 + X_4 = 1,$$

$$\langle r \rangle = X_1 r_{\mathrm{Mg}^{2+}} + X_2 r_{\mathrm{Fe}^{2+}} + X_3 r_{\mathrm{Mn}^{2+}} + X_4 r_{\mathrm{Ca}^{2+}},$$

$$r_{\mathrm{Mg}^{2+}} = 0.72\ \mathring{\mathrm{A}}, r_{\mathrm{Fe}^{2+}} = 0.77\ \mathring{\mathrm{A}},$$

$$r_{\mathrm{Mn}^{2+}} = 0.82\ \mathring{\mathrm{A}}, r_{\mathrm{Ca}^{2+}} = 1.00\ \mathring{\mathrm{A}},$$

$$V_{\text{unit cell}} = X_1 V_{\mathrm{MgCO}_3} + X_2 V_{\mathrm{FeCO}_3} + X_3 V_{\mathrm{MnCO}_3} + X_4 V_{\mathrm{CaCO}_3},$$

$$V_{\mathrm{MgCO}_3} = 277.69\ \mathring{\mathrm{A}}^3, V_{\mathrm{FeCO}_3} = 292.15\ \mathring{\mathrm{A}}^3,$$

$$V_{\mathrm{MnCO}_3} = 309.04\ \mathring{\mathrm{A}}^3, V_{\mathrm{CaCO}_3} = 376.60\ \mathring{\mathrm{A}}^3.$$

For comparison, data on the crystal structures of natural carbonates obtained from the literature are plotted in Fig. 3b, which approach the theoretical values estimated by the linear model. Some minor deviations could possibly be caused by other variables in the natural carbonates, such as composition measurement errors, lattice defects, or the distribution of misfit dislocations by various cationic substitutions. Besides, dolomite ($CaMg(CO_3)_2$) and kutnohorite ($CaMn(CO_3)_2$) were also plotted for comparison with the rigid model (Effenberger et al. 1981; Peacor et al. 1987). Interestingly, both accorded very well with the linear relationship. Thus, it is clear that the cell volume is not associated with the structure symmetry, such as the miscibility stacking or layer stacking of octahedrons, only depending on the substitution ionic radii. Eventually, the linear solid solution model is thought to be reasonable such that the unit cell volumes and theoretical densities of natural carbonates can be estimated conveniently by knowing their compositions. Figure 3c shows the variation in lattice parameters *a* and *c* as a function of ionic radii. Despite the unit cell volume obeying a perfectly linear rule overall, the *a* and *c* values of $MnCO_3$ and $CaCO_3$ diverge from the linear behavior

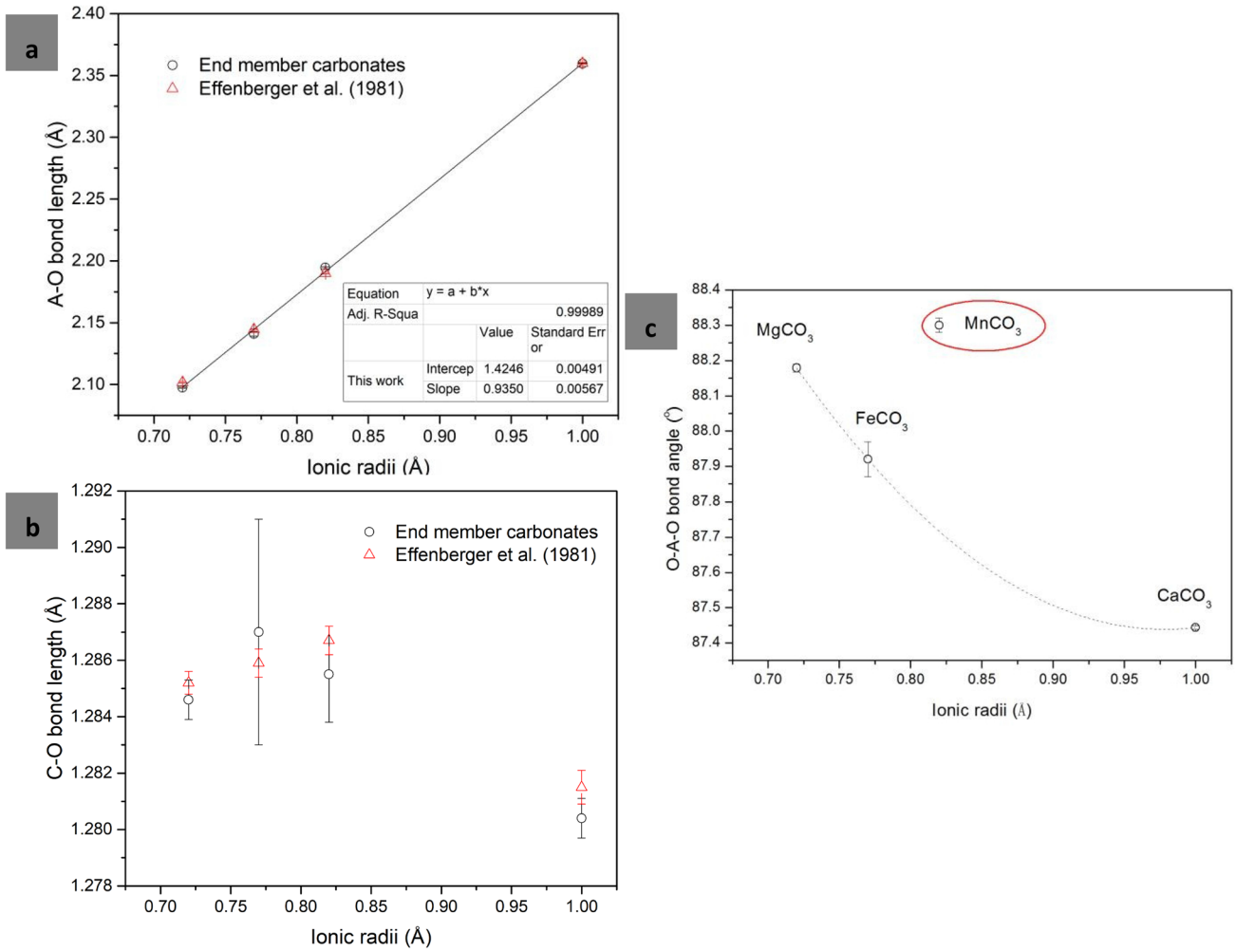

Fig. 4 Variation of bond length and bond angle with ionic radii, including A–O bond length (**a**), C–O bond length (**b**) as well as O–A–O bond angle (**c**) in calcite-type carbonates

constrained by $MgCO_3$ and $FeCO_3$, which is attributed to the different anisotropy resulting from the (AO_6) octahedron geometry.

The rigid body model is also adopted to explain the occurrence of a linear relationship between the A–O bond length and ionic radius, as shown in Fig. 4a, similar to that for unit cell volume. The C–O bond length varies little and nonlinearly with ionic radius, as given in Fig. 4b. Our results are very close to the riding model suggested by Effenberger et al. (1981) within the error range. The (AO_6) octahedral geometry is mainly dominated by cation substitution; in contrast, the C–O bonds behave more rigidly and are less affected. As shown in Fig. 4c, in a control group consisting of magnesite, siderite, and calcite with the same characteristics, the O–A–O bond angle decreases slightly with increases in A–O bond length. This reveals that the (AO_6) octahedron tends to tilt and deviate more than the regular octahedron while enlarging its volume. On the contrary, the (MnO_6) octahedron is anomalous and completely inconsistent with this rule. That is, the O–Mn–O bond angle of 88.30° is distinctly larger than that of others, such that the (MnO_6) octahedron tends more toward the regular octahedron.

Thermal expansivity of rhodochrosite crystals

As early as the 1970s, the thermal expansivity of rhodochrosite was investigated by high-T powder XRD at 28–265 °C (Rao and Murthy 1970). The volumetric thermal expansion coefficient $\alpha_V \approx 2.44 \times 10^{-5}$ °C^{-1} and the ratio $\alpha_c/\alpha_a = 31.0$. The thermal expansivity did not display good linear behavior and presented high anisotropy. Most recently, the thermal expansivity of rhodochrosite was re-investigated using high-T powder XRD at 25–400 °C (Li et al. 2019, in press). Using linear fitting, the thermal expansion coefficient was quantified as $\alpha_a = 4.18 \times 10^{-6}$ °C^{-1}, $\alpha_c = 2.50 \times 10^{-5}$ °C^{-1}, and

$\alpha_V = 3.35 \times 10^{-5}\ ^\circ C^{-1}$, and the ratio $\alpha_c/\alpha_a = 6.0$. The inconsistent could be possibly caused by measurements error and refinement process in powder XRD experiment. Even so, it is surprising that a remarkable α_c/α_a anisotropy was observed in the thermal expansivity of rhodochrosite, much larger than ~ 3.0 of magnesite (Markgraf and Reeder 1985). Ross (1997) reported that the compressibility of the (MgO_6) octahedron is nearly identical to that of magnesite. As an extension, it could be applied to the thermal expansion for calcite-type carbonates. Thus, the anomalous anisotropy may be associated with the geometric configuration (MnO_6) octahedron. To clarify these, we used impurity-free rhodochrosite as the standard sample to investigate the accurate thermal expansion by single-crystal XRD.

The coefficient of volume thermal expansion is strictly defined as

$$\alpha(T) = \frac{1}{V}\frac{\mathrm{d}V(T)}{\mathrm{d}T} = \alpha_0 + \alpha_1 T + \alpha_2 T^2 + \cdots$$

When T is not very high, the changes in volume with temperature exhibit a linear relationship. A mean linear expansion coefficient $\overline{\alpha}$ is used approximately, that is, $\alpha \approx \overline{\alpha} = \frac{1}{V_0}\frac{V(T)-V_0}{T-0} = \frac{K}{V_0}$, where K is the slope of the linear fit and V_0 is the volume at a temperature of 0 K. Figure 5a and Table 3 give the variations in lattice parameters a and c and unit cell volume with temperature, which can be linearly modeled as

$$a = 4.76821 + 2.4239 \times 10^{-5} T \left(\alpha_a = 5.08 \times 10^{-6}\ \mathrm{K}^{-1}\right),$$

$$c = 15.5627 + 2.8105 \times 10^{-4} T \left(\alpha_c = 18.06 \times 10^{-6}\ \mathrm{K}^{-1}\right),$$

$$V_{\text{unit cell}} = 306.41 + 8.73 \times 10^{-3} T \left(\alpha_{V\,\text{unit cell}} = 28.49 \times 10^{-6}\ \mathrm{K}^{-1}\right).$$

An approximate relationship of $\alpha_{V\text{unit cell}} \approx 2\alpha_a + \alpha_c$ for the rhombohedral structure was observed and the axial thermal expansivity presented substantial anisotropy. Calculated from α_c/α_a, the thermal expansion coefficient along the c-axis was 3.55 times greater than that along the a-axis, which is almost as the same situation as with compressibility (Merlini et al. 2015; Liu et al. 2016). Our values show a marked deviation from previous powder XRD results and the anisotropy is not as large; meanwhile, single crystal data are comparable to that of magnesite, which is thought to be more accurate and reliable.

Figure 5 gives the variations in bond length and angle as functions of temperature, and Table 4 shows the corresponding thermal expansion coefficient, together with those of magnesite and calcite for comparison. Here we omit siderite because there are not yet any studies on the thermal expansivity of siderite by single-crystal XRD. The Mn–O bond distance in rhodochrosite has a smaller thermal expansion coefficient ($\alpha_{A-O} = 12.14 \times 10^{-6}\ \mathrm{K}^{-1}$) with respect to the Mg–O bond distance in magnesite ($\alpha_{A-O} = 15.8 \times 10^{-6}\ ^\circ C^{-1}$) which is shorter at ambient conditions (see Table 4). Overall, the C–O bond length exhibits negative thermal expansion behavior with increasing temperature, whereas the values of rhodochrosite ($-3.67 \times 10^{-6}\ \mathrm{K}^{-1}$) and magnesite ($-4.6 \times 10^{-6}\ ^\circ C^{-1}$) are pretty close. The (AO_6) octahedron becomes more tilted with increased temperature, as evidenced by the slight decrease in the O–A–O bond angle: ~ 0.05°/100 K for rhodochrosite and ~ 0.07°/100 °C for magnesite. More importantly, the thermal expansivity of rhodochrosite and magnesite was found to agree with an approximate formula:

$$\alpha_V \approx \alpha_{AO6}/1.288 \approx 3 \times \alpha_{A-O}/1.288 = 2.329\alpha_{A-O}.$$

This indicates that the thermal expansion of the unit cell and (AO_6) octahedron is entirely determined by the A–O bond length.

As shown in Table 4, calcite is a special mineral with negative thermal expansion along the a-axis ($-2.8 \times 10^{-6}\ ^\circ C^{-1}$) caused by large thermal shrinkage of the C–O bond length ($-22.6 \times 10^{-6}\ ^\circ C^{-1}$). In comparison, rhodochrosite has positive thermal expansion along the a-axis ($5.08 \times 10^{-6}\ \mathrm{K}^{-1}$) with much smaller thermal shrinkage of the C–O bond length ($-3.67 \times 10^{-6}\ \mathrm{K}^{-1}$) than that of calcite. The ionic radius of Mn^{2+} (0.82 Å) is intermediate between those of Mg^{2+} (0.72 Å) and Ca^{2+} (1.00 Å). (Shannon and Prewitt 1969). Natural occurrences and experimental studies show that calcite and rhodochrosite can form a continuous solid solution ($Ca,Mn)CO_3$ at ambient conditions, called Mn-bearing calcite (Ozturk and Frakes 1995; Fan et al. 1999; Burke and Kemp 2002; Liu et al. 2016). Opposite thermal expansivity in calcite and rhodochrosite raises an interesting question; that is, there must be a critical Ca/Mn ratio in Mn-bearing calcite relating to the a-axis thermal expansion changing from negative to positive. In particular, this critical Mn-bearing calcite will exhibit thermal expansivity only along the c-axis while having no thermal response in the a–b plane. It is thought to be a new material with one-dimensional thermal expansivity and deserves further investigation in future.

Conclusion

The thermal expansion coefficient of impurity-free rhodochrosite was investigated by single-crystal XRD. It indicates that the thermal expansion is determined by Mn–O bond length, but not affected by the anomalous O–Mn–O bond angle. The anisotropy obtained by single-crystal XRD

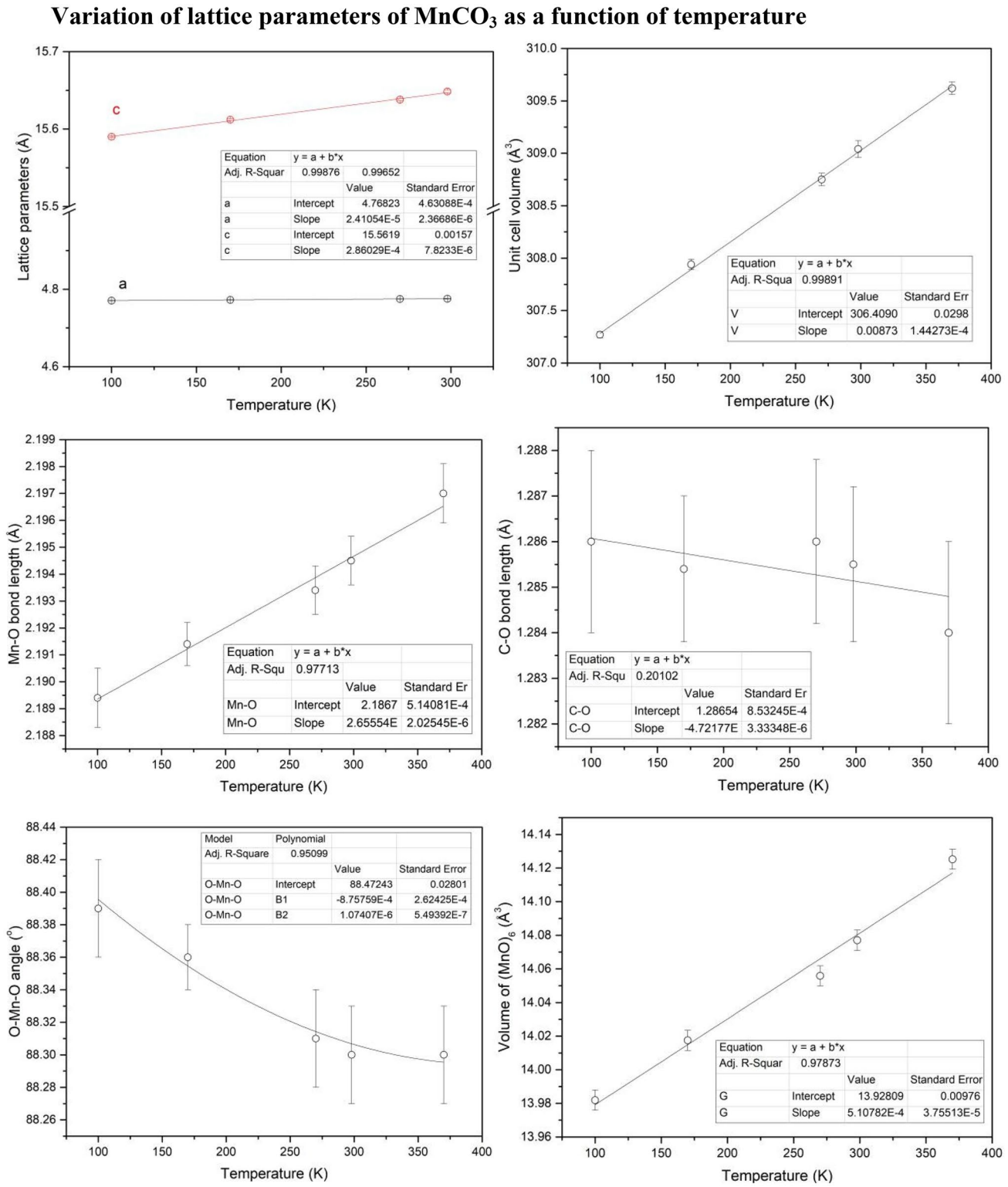

Fig. 5 Variation of lattice parameters of $MnCO_3$ as a function of temperature

Table 3 Single-crystal XRD of rhodochrosite at different temperatures

Temperature	100 K	170 K	270 K	298 K	370 K
a	4.7706 (3)	4.7724 (3)	4.7747 (4)	4.7754 (5)	4.7772 (4)
c	15.5900 (10)	15.6119 (12)	15.6379 (12)	15.6484 (18)	15.6659 (13)
$V_{\text{unit cell}}$	307.27 (3)	307.94 (5)	308.75 (6)	309.04 (8)	309.62 (6)
Mn–O	2.1894 (11)	2.1914 (8)	2.1934 (9)	2.1945 (9)	2.1970 (11)
C–O	1.2860 (20)	1.2854 (16)	1.2860 (18)	1.2855 (17)	1.2840 (20)
O1–Mn–O_2	88.39 (3)	88.36(2)	88.31 (3)	88.30 (3)	88.30 (3)
$V_{(MnO6)}$	13.982 (7)	14.008(6)	14.045 (6)	14.079 (6)	14.127 (7)

Table 4 Thermal expansion coefficient ($\times 10^{-6}$ K^{-1} or $^{o}C^{-1}$) of calcite-type ACO_3 carbonates at ambient pressure

ACO_3	A–O	O–A–O	V_{AO6}	C–O	*V*	*a*	*c*
MnCO3 This study	12.14	0.05°/100 K	36.67	− 3.67	28.49	5.08	18.06
$MgCO_3$* (Markgraf and Reeder 1985)	15.8	0.07°/100 ℃	46.9	− 4.6	36.4	6.75	22.9
$CaCO_3^*$ (Markgraf and Reeder 1985)	15.9	0.1°/100 ℃	47.2	− 22.6	26.7	− 2.8	32.3

$MgCO_3$* is natural magnesite: $Mg_{0.998}Ca_{0.002}CO_3$ and $CaCO_3$* is natural calcite: $Ca_{0.998}Mg_{0.002}CO_3$. (Markgraf and Reeder 1985)

data is close to that of magnesite and, therefore, anomalous anisotropy reported previously could be caused by low accuracy of refinement from powder XRD (Rao and Murthy 1970; Li et al. 2019, in press).

Likewise, previous studies report that the compressibility of calcite-type carbonates is related to the A–O bond length. As Martens et al. (1982) suggested, the compressibility coefficient can be completely determined by the A–O bond length, according to

$$\beta_{ACO_3}(\text{GPa}^{-1}) = 0.00097 \times (d_{A-O})^3.$$

Using this formula, the volume compressibility is calculated as 9.0×10^{-3} GPa^{-1} for magnesite and 9.5×10^{-3} GPa^{-1} for siderite, which agrees well with the experimental results of 9.0×10^{-3} GPa^{-1} for magnesite ($K_T = 111$ GPa, $K' = 4$; Ross 1997) and 9.7×10^{-3} GPa^{-1} for siderite ($K_T = 97.5$ GPa, $K' = 4$; Liang et al. 2018b). However, it cannot explain the lower compressibility of rhodochrosite when only considering the bond length effect. The compressibility of rhodochrosite could be consistent with that of the (MnO_6) octahedron, as it closely depends on the initial geometry of the (MnO_6) octahedron. We speculate that the anomalous O–Mn–O bond angle might play an important role in the lower compressibility of rhodochrosite. In this regard, the relationship between K_T and octahedron geometry warrants further investigation to clarify its compression mechanism.

Acknowledgements We appreciate two anonymous reviewers for their valuable comments and suggestions. We acknowledge Jung-Fu Lin from University of Texas at Austin for constructive discussion in carbonate minerals. This work was financially supported by Major State Research Development Program of China (2016YFC0601101), the National Science Foundation for Young Scientists of China (41802044), National Natural Fund of China (4160030283), the Strategic Priority Research Program (B) of Chinese Academy of Sciences (XDB 18010401), 135 Program of the Institute of Geochemistry (Y2ZZ041000), CAS, and the Western Light (Y8CR028).

References

Biellmann C, Gillet P, Guyot FO, Peyronneau J, Reynard B (1993) Experimental evidence for carbonate stability in the Earth's lower mantle. Earth Planet Sci Lett 118:31–41

Burke IT, Kemp AES (2002) Microfabric analysis of Mn-carbonate laminae deposition and Mn-sulfide formation in the Gotland Deep, Baltic Sea. Geochim Cosmochim Acta 66:1589–1600

Cerantola V, McCammon C, Kupenko I, Kantor I, Marini C, Wilke M, Ismailova L, Solopova N, Chumakov A, Pascarelli S, Dubrovinsky L (2015) High-pressure spectroscopic study of siderite ($FeCO_3$) with a focus on spin rossover. Am Mineral 100:2670–2681

Cerantola V, Bykova E, Kupenko I, Merlini M, Ismailova L, McCammon C, Bykov M, Chumakov AI, Petitgirard S, Kantor I, Svitlyk V, Jacobs J, Hanfland M, Mezouar M, Prescher C, Ruffer R, Prakapenka VB, Dubrovinsky L (2017) Stability of iron-bearing carbonates in the deep Earth's interior. Nat Commun 8:15960

Dasgupta R, Hirschmann MM (2010) The deep carbon cycle and melting in Earth's interior. Earth Planet Sci Lett 298:1–13

Duan J, Fu Y, Zhang Z, Ma X, Xiao J (2019) The metallogenic environment of the Dounan manganese deposit, Southeast Yunnan, China: evidence from geochemistry and Moesbauer spectroscopic. Acta Geochim 38:78–94

Effenberger H, Mereiter K, Zemann J (1981) Crystal structure refinements of magnesite, calcite, rhodochrosite, siderite, smithonite, and dolomite, with discussion of some aspects of the stereochemistry of calcite type carbonates. Zeitschrift fur Kristallographie 156:233–243

Fan D, Hein JR, Ye J (1999) Ordovician reef-hosted Jiaodingshan Mn–Co deposit and Dawashan Mn deposit, Sichuan Province, China. Ore Geol Rev 15:135–151

Farfan GA, Boulard E, Wang S, Mao WL (2013) Bonding and electronic changes in rhodochrosite at high pressure. Am Mineral 98:1817–1823

Fiquet G, Guyot F, Itie LP (1994) High-pressure X-ray diffraction study of carbonates: $MgCO_3$, $CaMg(CO_3)_2$, and $CaCO_3$. Am Mineral 79:15–23

Gillet P, Biellmann C, Reynard B, McMillan P (1993) Raman spectroscopic studies of carbonates part I: high-pressure and high-temperature behaviour of calcite, magnesite, dolomite and aragonite. Phys Chem Miner 20:1–18

Graf DL (1961) Crystallographic tables for the rhombohedral carbonates. Am Mineral 46:1283–1316

Hazen RM, Finger L (1982) Comparative crystal chemistry: temperature, pressure, composition and the variation of crystal structure. Wiley, New York, p 228

Hazen RM, Hemley RJ, Mangum AJ (2012) Carbon in Earth's interior: storage, cycling, and life. Eos Trans Am Geophys Union 93(2):17–18

Ishizawa N, Setoguchi H, Yanagisawa K (2013) Structural evolution of calcite at high temperatures: phase V unveiled. Sci Rep 3:2832

Isshiki M, Irifune T, Hirose K, Ono S, Ohishi Y, Watanuki T, Nishibori E, Takata M, Sakata M (2004) Stability of magnesite and its high-pressure form in the lowermost mantle. Nature 427:60–63

Javoy M (1997) The major volatile elements of the Earth: their origin, behaviour, and fate. Geophys Res Lett 24:177–180

Lavina B, Dera P, Downs RT, Prakapenka V, Rivers M, Sutton S, Nicol M (2009) Siderite at lower mantle conditions and the effects of the pressure-induced spin-pairing transition. Geophys Res Lett 36:L23306

Li R, Liang W, He H, Meng Y, Tang H (2019) The high-pressure synthesis and thermal expansivity investigation of carbonates solid solutions $Mg_{1-x}Mn_xCO_3$. High Temp High Press 48:367–380

Liang W, Li Z, Yin Y, Li R, Chen L, He Y, Dong H, Dai L, Li H (2018a) Single crystal growth, characterization and high-pressure Raman spectroscopy of impurity-free magnesite ($MgCO_3$). Phys Chem Miner 45:423–434

Liang W, Yin Y, Li Z, Li R, Lin L, He Y, Dong H, Li Z, Yan S, Zhai S, Li H (2018b) Single crystal growth, crystalline structure investigation and high-pressure behavior of impurity-free siderite ($FeCO_3$). Phys Chem Miner 45:831–842

Liang W, Chen L, Wang L, Yin Y, Li Z, Li H (2018c) High pressure synthesis of siderite ($FeCO_3$) and its thermal expansion coefficient. High Temp High Press 47:153–164

Lin J-F, Liu J, Jacobs C, Prakapenka VB (2012) Vibrational and elastic properties of ferromagnesite across the electronic spin-pairing transition of iron. Am Mineral 97:583–591

Litasov KD, Ohtani E (2009) Solidus and phase relations of carbonated peridotite in the system $CaO–Al_2O_3–MgO–SiO_2–Na_2O–CO_2$ to the lower mantle depths. Phys Earth Planet Inter 177:46–58

Liu L-G, Lin C-C, Yang Y-J (2001) Formation of diamond by decarbonation of $MnCO_3$. Solid State Commun 118:195–198

Liu J, Lin J-F, Mao Z, Prakapenka VB (2014) Thermal equation of state and spin transition of magnesiosiderite at high pressure and temperature. Am Mineral 99:84–93

Liu J, Caracas R, Fan D, Bobocioiu E, Zhang D, Mao WL (2016) High-pressure compressibility and vibrational properties of (Ca, Mn) C_{O3}. Am Mineral 101:2723–2730

Ma H, Xu Y, Huang K, Sun Y, Ke S, Peng Y, Shen B (2018) Heterogeneous Mg isotopic composition of the early Carboniferous limestone: implications for carbonate as a seawater archive. Acta Geochim 37:1–18

Markgraf SA, Reeder RJ (1985) High-temperature structure refinements of calcite and magnesite. Am Mineral 70:590–600

Martens R, Rosenhauer M, Gehlen KV (1982) Compressibilities of carbonates. In: Schreyer W (ed) High-pressure researches in geoscience. E. Schweizerbart'sche Verlagsbuchhandlung, Stuttgart, pp 215–222

Maslen EN, Streltsov VA, Streltsova NR (1995) Electron density and optical anisotropy in rhombohedral carbonates. III. Synchrotron X-ray studies of $CaCO_3$, $MgCO_3$ and $MnCO_3$. Acta Crystallogr B51:929–939

Megaw HD (1971) Crystal structures and thermal expansion. Mater Res Bull 6:1007–1018

Merlini M, Hanfland M, Gemmi M (2015) The $MnCO_3$-II high-pressure polymorph of rhodochrosite. Am Mineral 100:2625–2629

Merlini M, Sapelli F, Fumagalli P, Gatta GD, Lotti P, Tumiati S, Aabdellatief M, Lausi A, Plaisier J, Hanfland M, Crichton W, Chantel J, Guignard J, Meneghini C, Pavese A, Poli P (2016) High-temperature and high-pressure behavior of carbonates in the ternary diagram $CaCO_3–MgCO_3–FeCO_3$. Am Mineral 101:1423–1430

Oelkers EH, Cole DR (2008) Carbon dioxide sequestration a solution to a global problem. Elements 4:305–310

Ono S, Kikegawa T, Ohishi Y (2007) High-pressure transition of CaCO3. Am Mineral 92:1246–1249

Ozturk H, Frakes LA (1995) Sedimentation and diagenesis of an Oligocene manganese deposit in a shallow sub-basin of the Paratethys: Thrace Basin, Turkey. Ore Geol Rev 10:117–132

Peacor DR, Essene EJ, Gaines AM (1987) Petrologic and crystal-chemical implications of cation order-disorder in kutnahorite $CaMn(CO_3)_2$. Am Mineral 72:319–328

Rao KVK, Murthy KS (1970) Thermal expansion of manganese carbonate. J Mater Sci 5:82–83

Reeder RJ (1983) Crystal chemistry of the rhombohedral carbonates. In: Reeder RJ (ed) Carbonates: mineralogy and chemistry. Reviews in mineralogy, 11. Mineralogical Society of America, Washington, DC, pp 1–48

Reeder RJ, Dollase WA (1989) Structural variation in the dolomite-ankerite solid-solution series: an X-ray, Moessbauer, and TEM study. Am Mineral 74:1159–1167

Rosenberg PE (1963) Synthetic solid solutions in the systems $MgCO_3–FeCO_3$ and $MnCO_3–FeCO_3$. Am Mineral 48:1396–1400

Ross NL (1997) The equation of state and high-pressure behavior of magnesite. Am Mineral 82:682–688

Santillan J, Williams Q (2004) A high-pressure infrared and X-ray study of $FeCO_3$ and $MnCO_3$: comparison with $CaMg(CO_3)_2$-dolomite. Phys Earth Planet Inter 143–144:291–304

Seto Y, Hamane D, Nagai T, Fujino F (2008) Fate of carbonates within oceanic plates subducted to the lower mantle, and a possible mechanism of diamond formation. Phys Chem Miner 35:223–229

Shannon RD, Prewitt CT (1969) Effective ionic radii in oxides and fluorides. Acta Crystallogr A B25:925–946

Sheldrick GM (2008) Acta Crystallogr A 2008(64):112–122

Spivak A, Solopova N, Cerantola V, Bykova E, Zakharchenko E, Dubrovinsky L, Litvin Y (2014) Raman study of $MgCO_3–FeCO_3$ carbonate solid solution at high pressures up to 55 GPa. Phys Chem Miner 41:633–638

Suito K, Namba J, Horikawa T, Taniguchi Y, Sakurai N, Kobayashi M, Onodera A, Shimomura O, Kikegawa T (2001) Phase relations of $CaCO_3$ at high pressure and high temperature. Am Mineral 86:997–1002

Williams Q, Collerson B, Knittle E (1992) Vibrational spectra of magnesite ($MgCO_3$) and calcite-III at high pressures. Am Mineral 77:1158–1165

Zhang J, Martinez I, Guyot F, Gillet P, Saxena SK (1997) X-ray diffraction study of magnesite at high pressure and high temperature. Phys Chem Miner 24:122–130